Consistent modified gravity analysis of anisotropic galaxy clustering using BOSS DR11

Yong-Seon Song,[1] Atsushi Taruya,[2,3] Eric Linder,[4] Kazuya Koyama,[5] Cristiano G. Sabiu,[1] Gong-Bo Zhao,[6,5] Francis Bernardeau,[7,3] Takahiro Nishimichi,[3,7,8] and Teppei Okumura[3,*]

[1]*Korea Astronomy and Space Science Institute, Daejeon 305-348, Republic of Korea*
[2]*Yukawa Institute for Theoretical Physics, Kyoto University, Kyoto 606-8502, Japan*
[3]*Kavli Institute for the Physics and Mathematics of the Universe (WPI), The University of Tokyo Institutes*
for Advanced Study, The University of Tokyo, 5-1-5 Kashiwanoha, Kashiwa 277-8583, Japan
and Kavli Institute for the Physics and Mathematics of the Universe, Todai Institutes for Advanced Study,
the University of Tokyo, Kashiwa, Chiba 277-8583, Japan
[4]*Berkeley Lab and Berkeley Center for Cosmological Physics, University of California,*
Berkeley, California 94720, USA
[5]*Institute of Cosmology and Gravitation, University of Portsmouth,*
Portsmouth PO1 3FX, United Kingdom
[6]*National Astronomy Observatories, Chinese Academy of Science,*
Beijing 100012, People's Republic of China
[7]*CNRS and UPMC, UMR 7095, Institut dAstrophysique de Paris, F-75014, Paris, France*
[8]*CREST, JST, 4-1-8 Honcho, Kawaguchi, Saitama 332-0012, Japan*

We analyze the clustering of a cosmic large scale structure using a consistent modified gravity perturbation theory, accounting for anisotropic effects along and transverse to the line of sight. The growth factor has a particular scale dependence in $f(R)$ gravity and we fit for the shape parameter f_{R0} simultaneously with the distance and the large scale (general relativity) limit of the growth function. Using more than 690,000 galaxies in the baryon oscillation spectroscopy survey data release 11, we find no evidence for extra scale dependence, with the 95% confidence upper limit $|f_{R0}| < 8 \times 10^{-4}$. Future clustering data, such as from the dark energy spectroscopic instrument, can use this consistent methodology to impose tighter constraints.

PACS numbers: 98.80.-k, 04.50.Kd, 98.65.Dx

I. INTRODUCTION

The growth of large scale structure in the universe is a multifaceted probe of cosmology. The galaxy clustering pattern measures cosmic geometry through baryon acoustic oscillations, giving angular distances transverse to the line of sight and radial distance intervals, or the Hubble parameter, along the line of sight, and the ratio of the two known as the Alcock-Paczyński effect [1]. The evolution of the clustering amplitude provides the growth factor and the shape of the clustering correlation function or power spectrum depends on early universe conditions and later, scale dependent effects. In addition, redshift space distortions (RSD) cause anisotropy in the clustering between the transverse and radial directions, and this probes the velocity field and the law of gravity [2–7].

General relativity (GR) predicts scale independent growth in the linear perturbation regime and specific redshift distortion patterns, and so probing for scale dependence or distortion deviations can test the theory of gravity. Our aim is to investigate the general relativity cosmological framework by fitting the galaxy clustering data while allowing for scale dependence, and constrain such deviations. We are particularly motivated by scalar-tensor theories and use a perturbation theory template derived for $f(R)$ gravity. Scale dependence arises at length scales smaller than or of order the inverse of the scalaron mass $m = 1/\sqrt{3f_{RR}}$, where a subscript R denotes a derivative with respect to the Ricci scalar [8]. For GR, $f = R$ and so the scale dependence vanishes. This scale dependence was tested using the combination of cosmic microwave background (CMB) data and galaxy clustering spectra in the following work [9].

By employing the perturbation theory of Taruya *et al.* [10] that uses a resummed propagator to partially include nonperturbative and screening effects of the modified gravity, we can analyze the clustering correlation function to smaller scales than linear theory or simple perturbation calculations. We join this to our previous, substantially model independent approach of treating the background expansion in terms of the angular diameter distance and Hubble parameter [11–13], rather than assuming a dark energy model such as ΛCDM. Furthermore, we generalize the previous scale independent growth factor to two quantities: one scale independent (corresponding to the

*[*]ysong@kasi.re.kr

large scale limit of the growth factor) and one scale dependent (which can be thought of as characterizing the scalar-tensor modification, e.g. m or f_{R0}).

While we concentrate here on improving the RSD and galaxy clustering analysis for testing GR, various other methods have also been used. For example, the Planck collaboration has put constraints on a wide of range of modified gravity models using the Planck 2015 CMB data, combined with large scale structure observations [14]; the SDSS-III (BOSS) team has tested GR using the observed structure growth patterns [15–17]; the Wiggle-z team has tested modified gravity models [18,19]; and the CFHTLenS team employs the complementarity between weak gravitational lensing and RSD [20]. The abundance of clusters [21,22] and the cluster profiles [23,24] have also been used for gravity tests. For more recent observational tests of GR, see [25–32] and [33] for a review.

To focus on exploring the scale dependence, we use only the clustering data, from the Baryon Oscillation Spectroscopic Survey (BOSS) Data Release 11 (DR11) of the Sloan Digital Sky Survey 3 (SDSS3) [34,35]. This consists of about 690,000 galaxies over an effective volume of 6 Gpc³ with an effective redshift $z = 0.57$. We measure the two dimensional anisotropic correlation function as a function of transverse and radial separation between galaxies, and fit this to the redshift space distorted resummed perturbation theory. This comparison then imposes constraints on the cosmological and gravitational quantities, allowing us to test general relativity.

Section II describes the modified gravity theoretical approach, from the $f(R)$ gravity model to the resummed propagator and resulting perturbation theory to the prediction for the clustering correlation function. We also lay out our approach of splitting the growth function into scale

independent and dependent parts. In Sec. III A we discuss measurement of the anisotropic correlation function from the data and treatment of the covariance matrix. We verify in Sec. III B that we recover ΛCDM from ΛCDM simulated data. The comparison of the theory to the measurement is in Sec. III C and III D, where we analyze the fits to the cosmological quantities and their consistency with general relativity and ΛCDM. We summarize and conclude in Sec. IV.

II. THEORETICAL MODEL

A. $f(R)$ gravity model

We consider perturbations around the Friedman-Robertson-Walker universe described by the metric

$$ds^2 = -(1 + 2\Psi)dt^2 + a(t)^2(1 - 2\Phi)\delta_{ij}dx^i dx^j. \quad (1)$$

We will investigate modified gravity models that can be modeled by Brans-Dicke gravity on subhorizon scales. The metric perturbations and the scalar field perturbation $\phi = \phi_0 + \varphi$ obey the following equations in Fourier space [36]

$$-k^2\Psi = 4\pi Ga^2\rho\delta + \frac{1}{2}k^2\varphi, \quad (2)$$

$$(3 + 2\omega_{\rm BD})\frac{1}{a^2}k^2\varphi = 8\pi G\rho_m\delta - \mathcal{I}(\varphi), \quad (3)$$

$$\Phi - \Psi = \varphi, \quad (4)$$

where $\mathcal{I}$ represents the self-interaction, which can be expanded as [36]

$$\mathcal{I}(\varphi) = M_1(k)\varphi(k) + \frac{1}{2}\int \frac{d^3\boldsymbol{k}_1 d^3\boldsymbol{k}_2}{(2\pi)^3}\delta_D(\boldsymbol{k} - \boldsymbol{k}_{12})M_2(\boldsymbol{k}_1, \boldsymbol{k}_2)\varphi(\boldsymbol{k}_1)\varphi(\boldsymbol{k}_2)$$
$$+ \frac{1}{6}\int \frac{d^3\boldsymbol{k}_1 d^3\boldsymbol{k}_2 d^3\boldsymbol{k}_3}{(2\pi)^6}\delta_D(\boldsymbol{k} - \boldsymbol{k}_{123})M_3(\boldsymbol{k}_1, \boldsymbol{k}_2, \boldsymbol{k}_3)\varphi(\boldsymbol{k}_1)\varphi(\boldsymbol{k}_2)\varphi(\boldsymbol{k}_3), \quad (5)$$

where $\boldsymbol{k}_{ij} = \boldsymbol{k}_i + \boldsymbol{k}_j$ and $\boldsymbol{k}_{ijk} = \boldsymbol{k}_i + \boldsymbol{k}_j + \boldsymbol{k}_k$. We treat the matter fluctuations δ as a pressureless fluid flow, whose evolution equation is given by

$$\frac{\partial\delta}{\partial t} + \frac{1}{a}\nabla \cdot [(1 + \delta)\mathbf{v}] = 0, \quad (6)$$

$$\frac{\partial\mathbf{v}}{\partial t} + H\mathbf{v} + \frac{1}{a}(\mathbf{v} \cdot \nabla) \cdot \mathbf{v} = -\frac{1}{a}\nabla\Psi. \quad (7)$$

We will assume the irrotationality of fluid quantities and express the velocity field in terms of the velocity divergence $\Theta = \nabla \cdot \mathbf{v}/(aH)$.

In order to develop the template for the redshift space power spectrum, we need to specify the interaction term $\mathcal{I}$. We consider $f(R)$ models as a representative class of models where the linear growth function is scale dependent. $f(R)$ gravity models are described by the action

$$S = \int d^4x\sqrt{-g}f(R) + \int d^4x\sqrt{-g}\mathcal{L}_m. \quad (8)$$

We consider the function $f(R)$ given by the lowest order expansion in the small quantity $|f_{R0}| \ll 1$,

$$f(R) = -2\kappa^2 \rho_\Lambda + |f_{R0}| \frac{\bar{R}_0^2}{R}, \qquad (9)$$

general to many $f(R)$ models that are observationally viable. Here ρ_Λ is the constant energy density and $\bar{R}_0$ is the background curvature at present time. For small $|f_{R0}|$, the background expansion in this Ansatz can be approximated as the one in the ΛCDM model.

The scalar field perturbation is given by

$$\varphi = f_R - \bar{f}_R, \qquad (10)$$

where $f_R = df/dR$ and the bar indicates that the quantity is evaluated on the background. $f(R)$ gravity models are equivalent to Brans-Dicke gravity with $\omega_{BD} = 0$ and the interaction term $\mathcal{I}$ is given by

$$\mathcal{I} = \delta R \equiv R(f_R) - R(\bar{f}_R). \qquad (11)$$

Thus the coupling functions M_n are

$$M_n = \frac{d^n \bar{R}(f_R)}{df_R^n}, \qquad (12)$$

so Eq. (9) gives

$$M_1 = \frac{1}{2} \frac{1}{|f_{R0}|} \frac{\bar{R}^3}{\bar{R}_0^2}. \qquad (13)$$

By linearizing the evolution equations, the solution for the gravitation potential is given by

$$k^2 \Psi = -4\pi G \left(\frac{4 + M_1 a^2/k^2}{3 + M_1 a^2/k^2} \right) a^2 \rho_m \delta. \qquad (14)$$

On scales larger than the Compton wavelength of the scalar field, $m^{-1} = (3/M_1)^{1/2} = \sqrt{3f_{RR}}$, the scalar field does not propagate and we recover ΛCDM. On the other hand, on small scales, gravity is enhanced: $G_{\text{eff}} \to (4/3)G$.

Combining this with the energy momentum conservation equations, we obtain the equation that determines the linear growth factor $D_+^\delta(k, t)$,

$$\mathcal{L}D_+^\delta = 0, \quad \mathcal{L} = \frac{d^2}{dt^2} + 2H\frac{d}{dt} - 4\pi G \left(\frac{4 + M_1 a^2/k^2}{3 + M_1 a^2/k^2} \right) \rho_m. \qquad (15)$$

The growth function D_+^δ and the growth rate $D_+^\Theta \equiv dD_+^\delta/d\log a$ are also scale dependent. We introduce the following parametrization of the growth rates

$$D_+^\delta(k, t) = G_\delta(t) F_\delta(k, t; M_1),$$
$$D_+^\Theta(k, t) = G_\Theta(t) F_\Theta(k, t; M_1), \qquad (16)$$

where we defined $F_\delta(k, t; M_1)$ and $F_\Theta(k, t; M_1)$ so that $D_+^\delta(k, t) \to G_\delta(t)$ and $D_+^\Theta(k, t) \to G_\Theta(t)$ in the limit of $k \to 0$. Since we recover ΛCDM in the $k \to 0$ limit, G_δ and G_Θ are determined by the usual cosmological parameters and they are independent of $|f_{R0}|$. On the other hand, the scale dependence is controlled by M_1 in Eq. (14), which is determined by $|f_{R0}|$ and the cosmological parameters.

We will find solutions for δ and θ by solving Eqs. (2), (3), (6), (7) using perturbation theory. Once the nonlinearity becomes important, the nonlinear self-interactions $M_{i>1}$ will suppress the scalar field interactions by the chameleon mechanism. This effect is included perturbatively in our approach.

B. RSD model for $f(R)$ gravity models

The anisotropy of galaxy clustering is now recognized as a useful probe of gravity on cosmological scales. This is because the anisotropic clustering signal contains information on both the cosmic expansion and growth of structure, through the Alcock-Paczynski effect and RSD. In principle, these two effects are simply described by the mapping formula from the statistically isotropic frame, however modeling the RSD effect is rather complex because of the nonlinear and stochastic nature of the mapping. As a result, the applicable range of the linear theory prediction is quite limited. Even at the largest scales accessible by future galaxy surveys, a proper account of the nonlinearity is crucial for a robust test of gravity.

Here, we will adopt an improved model of RSD by Ref. [37] for the theoretical template of the redshift-space correlation function. While this model has been originally proposed to characterize the matter power spectrum in GR, the assumptions and propositions behind the model prescription do not rely on any specific gravitational theory. Thus it can apply to any model of modified gravity. Indeed, the model has been tested against the dark matter simulation of the $f(R)$ gravity model, where a good agreement with N-body results was found [38]. One important remark is that the dynamics of density and velocity fields in modified gravity can be different from GR, and each building block in the RSD model needs to be carefully computed, taking a proper account of the modification of (non)linear gravitational growth, which we will describe below (see also Appendix). This is what we refer to as a consistent analysis of modified gravity.

Employing the linear bias prescription, the improved model of RSD is given in Fourier space as function of wave number k and directional cosine $\mu = k_z/k$ with k_z being line-of-sight component of k:

$$\tilde{P}(k, \mu) = \{b^2 P_{\delta\delta}(k) + 2\mu^2 b G_\Theta P_{\delta\Theta}(k) + \mu^4 G_\Theta^2 P_{\Theta\Theta}(k)$$
$$+ A(k, \mu; b, G_\Theta) + B(k, \mu; b, G_\Theta)\}$$
$$\times D_{\text{FoG}}(k\mu\sigma_p), \qquad (17)$$

where b is the linear bias parameter. (See Sec. III C for a more sophisticated treatment.) The G_Θ is the parameter characterizing the growth of structure introduced in Eq. (16). The functions $P_{\delta\delta}$, $P_{\Theta\Theta}$ and $P_{\delta\Theta}$ are, respectively, the auto-power spectra of density and velocity-divergence fields, and their cross-power spectrum. The function $D_{\rm FoG}$ characterizes the suppression of the power spectrum due to the virialized random motion of galaxies [39–41], for which we assume the Gaussian form:

$$D_{\rm FoG}(x) = e^{-x^2}. \qquad (18)$$

Since the suppression of the power spectrum basically comes from the galaxies sitting in a halo, we shall treat σ_p in the damping function $D_{\rm FoG}$ as a free parameter.

In Eq. (17), the main characteristic is the $A(k, \mu)$ and $B(k, \mu)$ terms, which represent the higher-order coupling between density and velocity fields. These have been derived on the basis of the low-k expansion from the exact expression for the redshift-space power spectrum, expressed as:

$$A = b^3 \sum_{n=1}^{3} \sum_{a,b=1}^{2} \mu^{2n} \left(\frac{G_\Theta}{b}\right)^{a+b-1} \frac{k^3}{(2\pi)^2} \int_0^\infty dr \int_{-1}^1 dx$$
$$\times \{A_{ab}^n(r,x)B_{2ab}(\boldsymbol{p}, \boldsymbol{k}-\boldsymbol{p}, -\boldsymbol{k})$$
$$+ \tilde{A}_{ab}^n(r,x)B_{2ab}(\boldsymbol{k}-\boldsymbol{p}, \boldsymbol{p}, -\boldsymbol{k})\}, \qquad (19)$$

$$B = b^4 \sum_{n=1}^{4} \sum_{a,b=1}^{2} \mu^{2n} \left(-\frac{G_\Theta}{b}\right)^{a+b} \frac{k^3}{(2\pi)^2} \int_0^\infty dr \int_{-1}^1 dx$$
$$\times B_{ab}^n(r,x) \frac{P_{a2}(k\sqrt{1+r^2-2rx})P_{b2}(kr)}{(1+r^2-2rx)^a}, \qquad (20)$$

where $r = p/k$ and $x = \boldsymbol{k} \cdot \boldsymbol{p}/(kp)$. Here, the functions P_{ab} and B_{abc} are the power spectrum and bispectrum of the two-component multiplet $\Psi_a = (\delta, \Theta)$. The nonvanishing coefficients, A_{ab}^n, $\tilde{A}_{ab}^n$, and B_{ab}^n, are those presented in Sec. III-B2 of Ref. [42] and Appendix of Ref. [37], respectively.

In calculation of the redshift-space power spectrum, we need to properly take into account the effect of nonlinear gravitational evolution in each term of Eq. (17). Since the standard perturbation theory (PT) [43] is known to produce an ill-behaved expansion leading to unwanted UV behavior, we shall apply the resummed perturbation theory called RegPT, which has been formulated in Ref. [44] and been later extended in Ref. [10] to the modified gravity models. Following the prescription described in [10], we compute the power spectra $P_{XY}(k)$ as well as the A and B terms, including consistently the nonlinear corrections up to the one-loop order in the $f(R)$ gravity model. The explicit expressions for statistical quantities, necessary for a

consistent one-loop calculation of the redshift-space power spectrum, are summarized in Appendix A.

In the cosmological analysis in Sec. III, we will consider the following two cases, which can be thought of as fixing the expansion and large scale growth histories, or allowing them to vary. In the first case, we will fix all the cosmological parameters in the template by a fiducial cosmology and vary $|f_{R0}|$, the linear bias b and the velocity dispersion σ_p. This corresponds to fixing G_δ, G_Θ and the amplitude of the initial spectrum to those determined by the fiducial cosmology.

In the second case, we allow G_Θ to float by varying $\Omega_\Lambda \equiv \rho_\Lambda/3H_0^2$ where H_0 is the present day Hubble constant in the flat universe. Note that with the variation of Ω_Λ, the amplitude of the growth function D_+^δ (G_δ) as well as the shape of the growth function (F_δ) and growth rate (F_Θ) are also changed through the mass parameter M_1 [see Eq. (15)]. In practice, however, we see from Fig. 1 that the dependence of the shapes F_δ and F_Θ on Ω_Λ are very weak. Further, the change of G_δ is degenerate with the linear bias b in the linear regime. Although the one-loop terms break the degeneracy, this effect is small in the regime of our interest. Hence, in the second case, we vary the scale independent growth rate G_Θ and the linear bias in the PT template, and introduce a new parameter

$$G_b(t) \equiv bG_\delta(t), \qquad (21)$$

to represent the combined effect of the variation of b and G_δ. Then G_δ and the initial amplitude of the power spectrum are formally held fixed.

C. Correlation function $\xi(\sigma, \pi)$ in $f(R)$ gravity

The two-point correlation function of galaxy clustering in the redshift space, ξ, is described by a function of σ and π, where σ and π are the transverse and the radial directions with respect to the observer. From the power spectrum $\tilde{P}(k, \mu)$, we can compute the correlation function $\xi(\sigma, \pi)$ by Fourier transformation. The correlation function is generally expanded as

$$\xi(\sigma, \pi) = \int \frac{d^3k}{(2\pi)^3} \tilde{P}(k, \mu)e^{i\boldsymbol{k}\cdot\boldsymbol{s}}$$
$$= \sum_{\ell:\,\text{even}} \xi_\ell(s)\mathcal{P}_\ell(\nu), \qquad (22)$$

with $\mathcal{P}_\ell$ being the Legendre polynomials. Here, we defined $\nu = \pi/s$ and $s = (\sigma^2 + \pi^2)^{1/2}$. The moments of the correlation function, $\xi_\ell(s)$, are defined in [11]. The contributions from moments higher than $\ell = 8$ will be ignored in our analysis because we are only interested in quasinonlinear scales where perturbation theory is applicable.

We compute theoretical templates for the moments $\xi_\ell(s)$ using the power spectrum given by Eq. (17). The shape of
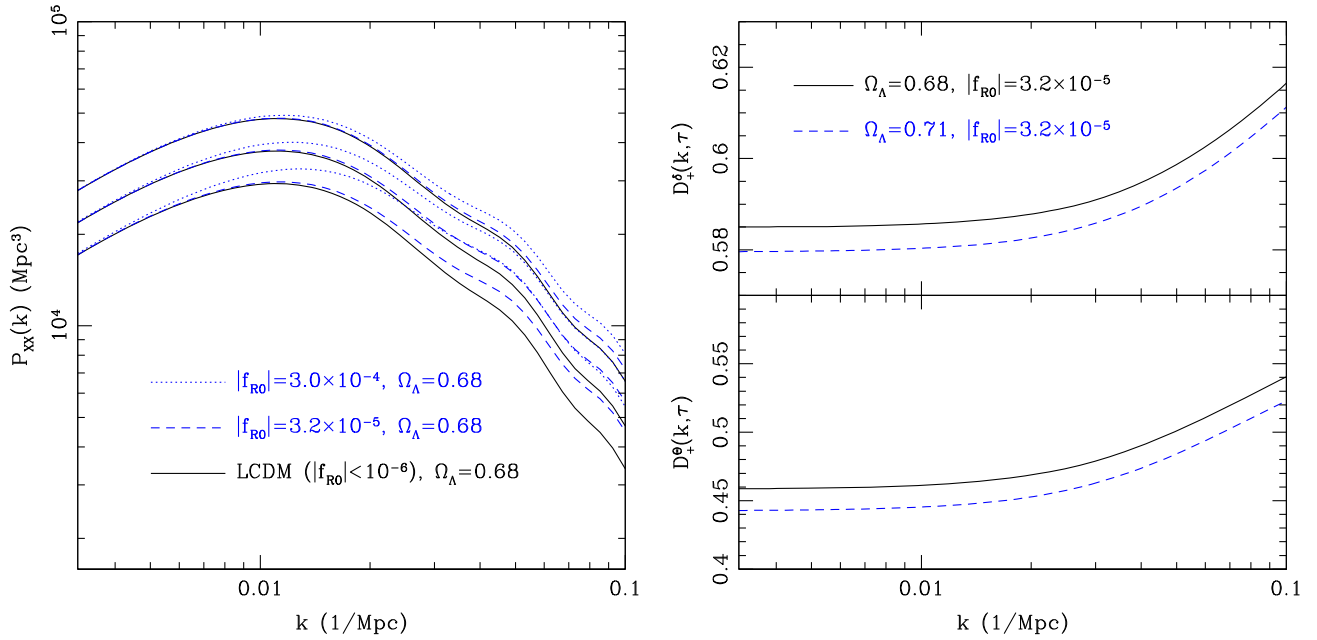
FIG. 1 (color online). (Left panel) The linear power spectra $P_{\delta\delta}(k)$, $P_{\delta\Theta}(k)$ and $P_{\Theta\Theta}(k)$ from top to bottom. The power spectra of the ΛCDM model are presented as black solid curves, and the power spectra of $f(R)$ gravity models with $|f_{R0}| = 3.2 \times 10^{-5}$ and $|f_{R0}| = 3.0 \times 10^{-4}$ are presented as blue dashed and dotted curves, respectively. The results are evaluated at redshift $z = 0.57$. (Right panel) The growth functions D_+^{δ} and D_+^{Θ} have a scale independent amplitude, depending on Ω_Λ (taking fixed primordial amplitude), and scale dependent shape, depending on $|f_{R0}|$. The results in each subpanel are shown at $z = 0.57$ for $|f_{R0}| = 3.2 \times 10^{-5}$, and $\Omega_\Lambda = 0.68$ (black solid curves) and 0.71 (blue dashed curves).

the initial spectra and the growth functions, G_δ and G_Θ, are given by the best fit ΛCDM model from Planck 2013 [45]. We provide multiple templates with various $|f_{R0}| = (0, 10^{-6}, 3.2 \times 10^{-6}, 10^{-5}, 3.2 \times 10^{-5}, 10^{-4}, 3.2 \times 10^{-4}, 10^{-3}, 3.2 \times 10^{-3})$. For other values of $|f_{R0}|$, we interpolate these templates.

We now study the variation of $\xi(\sigma, \pi)$ due to the change of the growth function and growth rate. This variation was studied in the case of scale independent growth functions in [11] by varying $G_\delta(t)$ and $G_\Theta(t)$ in the RegPT template for ΛCDM. Following this approach, we first study the impact of having a scale dependent growth function or growth rate. For this purpose, we compute the correlation function $\xi(\sigma, \pi)$ using a ΛCDM template and replace the growth function D_+^{δ} or growth rate D_+^{Θ} by that in $f(R)$ gravity with $|f_{R0}| = 3.2 \times 10^{-5}$ and $|f_{R0}| = 3.0 \times 10^{-4}$.

For the scale dependent growth function D_+^{δ}, the variation of $\xi(\sigma, \pi)$ with a small $|f_{R0}| = 3.2 \times 10^{-5}$ is similar to the case of a scale independent enhancement of the growth function studied in [11]. Peak points on the BAO ring represented by a thick black solid curve in Fig. 2 move coherently along the circle in an anticlockwise direction. The blue dashed contours in the left panel of Fig. 2 represent this variation. However, $\xi(\sigma, \pi)$ with a larger $|f_{R0}| = 3.0 \times 10^{-4}$ varies differently from the scale independent case. Peak points on the BAO ring remain the

same, while minima of BAO are deepened, shown as blue dotted contours in the same panel.

Next, we consider the variation of $\xi(\sigma, \pi)$ due to the scale dependent growth rate D_+^{Θ}. In the case of the scale independent growth rate, if G_Θ increases or decreases, the anisotropic effects from higher order moments are visible in the plot of $\xi(\sigma, \pi)$. The location of the crossing points between the contour levels and the BAO ring (thick solid) shifts clockwise or anticlockwise slightly. The blue dashed contours in the right panel of Fig. 2 represent the variation of $\xi(\sigma, \pi)$ with ΔD_+^{Θ} for $|f_{R0}| = 3.2 \times 10^{-5}$ and $|f_{R0}| = 3.0 \times 10^{-4}$. For $|f_{R0}| = 3.0 \times 10^{-4}$, we can see that the peak positions are "squeezed" along the BAO ring.

Having shown the individual effects of a scale dependent growth function and growth rate on the correlation function, we now present the correlation function $\xi(\sigma, \pi)$ in $f(R)$ gravity models. In Fig. 3, the correlation function with $|f_{R0}| = 3.2 \times 10^{-5}$ and $|f_{R0}| = 3.0 \times 10^{-4}$ are plotted as black dashed and black dotted contours, respectively. There is no variation of $\xi(\sigma, \pi)$ up to $|f_{R0}| \lesssim 10^{-6}$, and the correlation function is effectively equivalent to that of ΛCDM. When $|f_{R0}|$ increases to $|f_{R0}| \sim 10^{-4}$, we observe the deviation of $\xi(\sigma, \pi)$ from ΛCDM and this deviation can be understood as the combined effect of the scale dependent growth function and growth rate shown in Fig. 2.
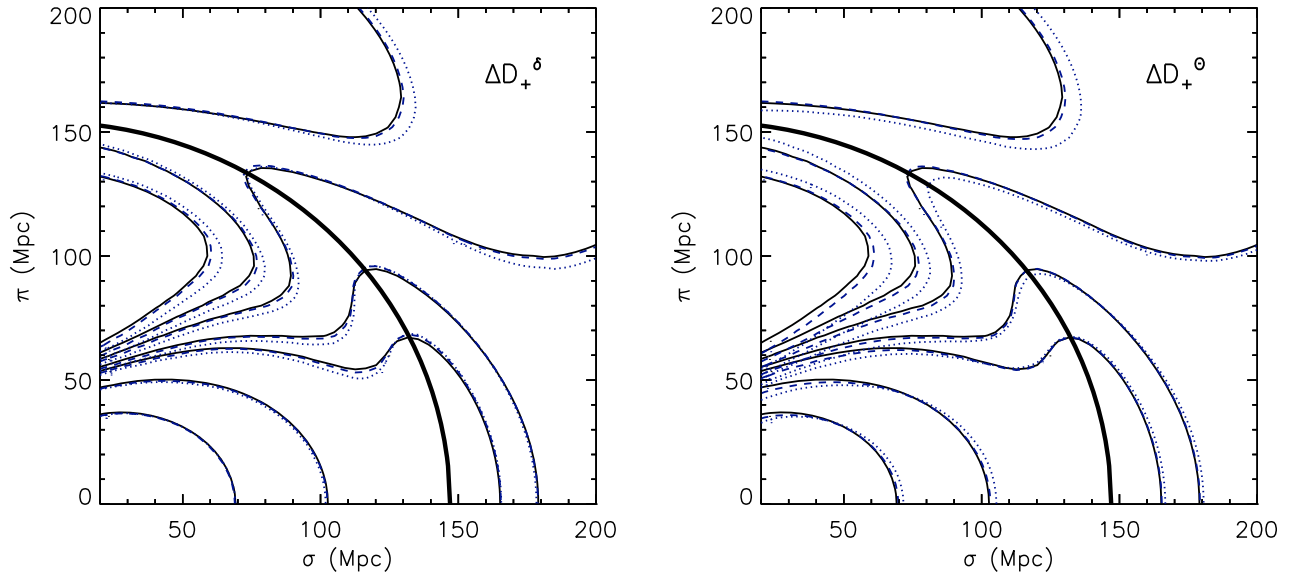
FIG. 2 (color online).   (Left panel) The correlation function $\xi(\sigma, \pi)$ of the ΛCDM model is shown as black solid contours. Blue dashed and dotted contours represent $\xi(\sigma, \pi)$ of the ΛCDM model in which D_+^δ is replaced by that of $f(R)$ gravity models with $|f_{R0}| = 3.2 \times 10^{-5}$ and $|f_{R0}| = 3.0 \times 10^{-4}$, respectively. The thick solid circle represents the BAO ring. The levels of contours are given by $(-0.005, -0.0025, -0.004, 0.003, 0.005, 0.016, 0.05)$ from outer to inner contours. (Right panel) Black solid contours represent $\xi(\sigma, \pi)$ of the ΛCDM model, and blue dashed and dotted contours represent $\xi(\sigma, \pi)$ of the ΛCDM model in which D_+^Θ is replaced by that of $f(R)$ gravity models of $|f_{R0}| = 3.2 \times 10^{-5}$ and $|f_{R0}| = 3.0 \times 10^{-4}$, respectively.
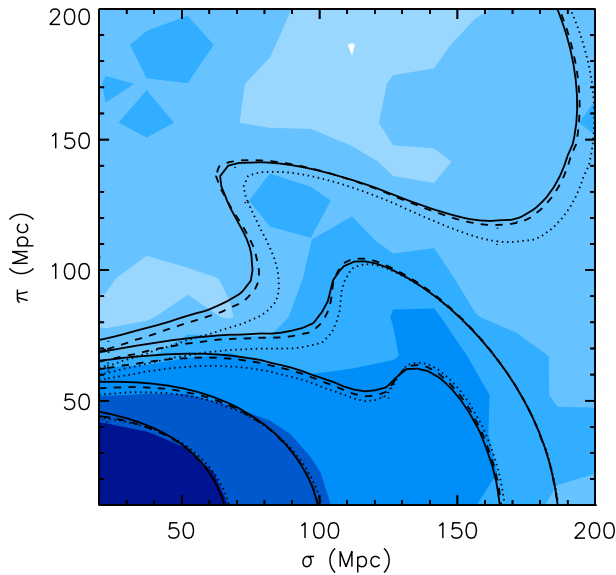
FIG. 3 (color online).   The best fit correlation function $\xi(\sigma, \pi)$ of ΛCDM (black solid unfilled contours) and the correlation function of $f(R)$ gravity models with $|f_{R0}| = 3.2 \times 10^{-5}$ (black dashed unfilled contours) and 3.0×10^{-4} (dotted unfilled contours). The blue filled contours represent the measured $\xi(\sigma, \pi)$ from the DR11 CMASS data. The levels of contours are given by $(-0.001, 0.002, 0.005, 0.016, 0.05)$ from the outer to inner contours.

III. METHODOLOGY AND RESULTS

The observed clustering of galaxies in redshift space not only probes the density and velocity fields, i.e. the growth and gravity as discussed in the previous section, but also

provides a useful tool to determine both the transverse and radial distances by exploiting the Alcock–Paczyński effect and the BAO scale. In galaxy redshift surveys, each galaxy is located by its angular coordinates and redshift. However, the correlation function, $\xi(\sigma, \pi)$, is measured in comoving distances. Therefore a fiducial cosmological model is required for conversion into comoving space. We use the best fit ΛCDM universe to Planck 2013 data. The conversion depends on the transverse and radial distances involving D_A and H^{-1}. Instead of recreating the measured correlation function in comoving distances for each different model, we create the fiducial maps from the theoretical correlation function by rescaling the transverse and radial distances using D_A and H^{-1} and fit them to the observed correlation function. Therefore, when we fit the measured $\xi(\sigma, \pi)$, the two distance parameters of (D_A, H^{-1}) are added to the structure formation parameter set of $\{G_\delta, G_\Theta, \sigma_p, |f_{R0}|, \sigma_p\}$ discussed in Sec. II B.

A. Measured $\xi(\sigma, \pi)$ using DR11

Our measurements are based on those previously presented in [13] which follows a similar procedure to [12].

Briefly, in our analysis we utilize data release DR11 of the Baryon Oscillation Spectroscopic Survey [BOSS; [46–48]] which is part of the larger Sloan Digital Sky Survey [SDSS; [49,50]] program. From DR11 we focus our analysis on the *Constant Stellar Mass Sample* (CMASS) [51], which contains 690,826 galaxies and covers the redshift range $z = 0.43$–0.7 over a sky area of $\sim 8,500$ square degrees with an effective volume of

$V_{\mathrm{eff}} \sim 6.0$ Gpc^3. The CMASS galaxy sample is composed primarily of bright, central galaxies, resulting in a highly biased ($b \sim 2$) selection of mass tracers [52].

The redshift-space two-dimensional correlation function $\xi(\sigma, \pi)$ of the BOSS DR11 galaxies was computed using the standard Landy-Szalay estimator [53]. In the computation of this estimator we used a random point catalogue that constitutes an unclustered but observationally representative sample of the BOSS CMASS survey and contains ~ 50 times as many randoms as we have galaxies.

The covariance matrix was obtained from 600 mock catalogues based on second-order Lagrangian perturbation theory (2LPT) [54,55]. The mocks reproduce the same survey geometry and number density as the CMASS galaxy sample. We obtain the covariance matrix using the same treatment presented in our previous works [12,13].

We calculate the correlation function in 225 bins spaced by $10 \, h^{-1}$ Mpc in the range $0 < \sigma, \pi < 150 h^{-1}$ Mpc. However, at small scales, if the nonperturbative effect of FoG is underestimated, then the residual squeezing can be misinterpreted as a variation in G_θ or indeed f_{R0}. We expect the FoG effect to be increasingly important at smaller scales, and so these measurements may be at risk of misestimation. We therefore impose a conservative cut on the measurements, excluding $\sigma_{\mathrm{cut}} < 40 \, h^{-1}$ Mpc and $s_{\mathrm{cut}} < 50 \, h^{-1}$ Mpc [12]. Indeed, [12] showed that cosmological parameter bias began to occur at smaller scales.

This reduces the number of measurement bins in σ and π to $N_{\mathrm{bins}} = 163$.

B. Tests of theoretical templates

When the conservative cutoff scales of $\sigma_{\mathrm{cut}} = 40 \, h^{-1}$ Mpc and $s_{\mathrm{cut}} = 50 \, h^{-1}$ Mpc are used for the analysis, the effective range of scale in Fourier space becomes $k < 0.1$ Mpc^{-1}. The power spectra of ΛCDM and $f(R)$ gravity models are presented in this range of scale in Fig. 1. For the clustering scales considered in this likelihood analysis, there are no deviations from ΛCDM. This implies that $f(R)$ gravity models with $\log|f_{R0}| \lesssim -6$ are effectively equivalent to ΛCDM in this analysis. We take a uniform prior on $\log|f_{R0}|$ between -7 and -3.

We first test our pipeline of analysis by checking whether it is possible to recover the ΛCDM limit $\log|f_{R0}| \lesssim -6$ using the mock catalogues based on ΛCDM. We use the 611 CMASS mock catalogues to measure central values of $\xi(\sigma, \pi)$ and fit our theoretical $f(R)$ templates to the observed correlation function. The measured likelihood function of $\log|f_{R0}|$ is presented as a blue dotted curve in the right panel of Fig. 4. The best fit $\log|f_{R0}|$ indeed lies within the ΛCDM limit of $\log|f_{R0}| \lesssim -6$. There are no mock galaxy catalogues based on $f(R)$ gravity available so we are not able to fully test our theoretical templates away from the ΛCDM limit. The perturbation theory predictions for the redshift space power spectrum in Fourier space
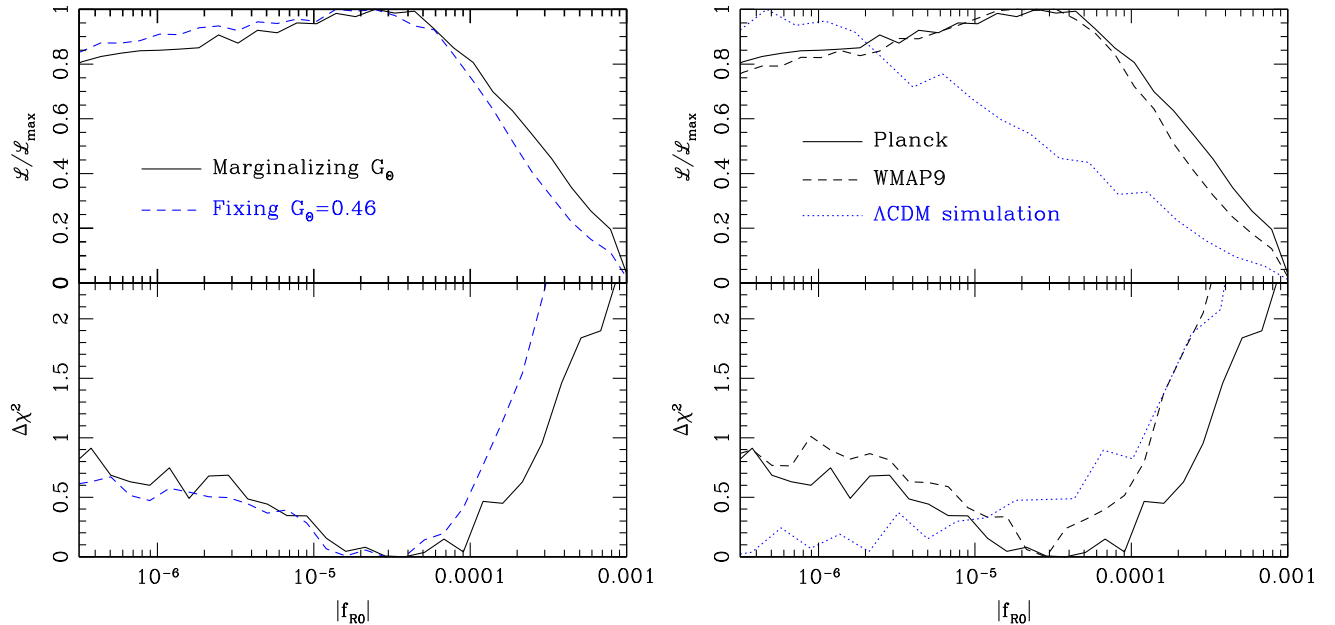

FIG. 4 (color online). The measured constraints on f_{R0}, and their robustness to various tests, are presented. The measured likelihood function appears in the top panels and the measured difference of χ^2 is in the bottom panels. (Left panel) Results marginalizing over the scale independent growth rate G_Θ are shown by the black solid curve, while the constraints fixing $G_\Theta = 0.46$, given by the Planck concordance ΛCDM model, are blue dashed curves. The results for f_{R0} do not depend appreciably on the scale independent behavior. (Right panel) The results also do not depend significantly on whether the initial power spectrum $P(k)$ used matches the Planck (black solid) or WMAP9 (black dashed) model. The blue dotted curve represents the results from analyzing galaxy clustering from ΛCDM mock catalogues, verifying that $|f_{R0}| \to 0$ is recovered in this case.

TABLE I. The Planck best-fit ΛCDM predictions and the measured values with their 1-σ confidence level errors are shown for the parameters $D_A, H^{-1}, G_b, G_\Theta, \sigma_p, \log|f_{R0}|$. The Planck ΛCDM data does not predict the phenomenological parameters G_b and σ_p. The last two columns show the measured values in the test cases when G_Θ is fixed to the Planck prediction 0.46, or $f_{R0} = 0$, respectively.

Parameters	Planck	Measurements	Fixed $G_\Theta = 0.46$	Fixed $|f_{R0}| = 0$
D_A (Mpc)	1397.5	$1428.0^{+30.1}_{-28.1}$	$1424.3^{+30.0}_{-27.8}$	$1422.6^{+27.3}_{-31.7}$
H^{-1} (Mpc)	3240.1	$3157.5^{+190.6}_{-176.1}$	$3179.3^{+198.1}_{-185.6}$	$3218.3^{+200.3}_{-173.3}$
G_b	–	$1.13^{+0.09}_{-0.08}$	$1.10^{+0.06}_{-0.06}$	$1.15^{+0.09}_{-0.08}$
G_Θ	0.46	$0.39^{+0.09}_{-0.09}$	0.46 (fixed)	$0.41^{+0.09}_{-0.09}$
σ_p (Mpc)	–	$10.6^{+4.5}_{-4.6}$	$11.7^{+3.9}_{-4.1}$	$9.3^{+5.3}_{-5.6}$
$\log|f_{R0}|$	–	$-4.5^{+0.96(1.4)}_{[\text{prior}]}$	$-4.5^{+0.63(0.90)}_{[\text{prior}]}$	–
$\chi^2_{\min}$	–	126.9	127.6	127.7

were, however, tested against N-body simulations for $f(R)$ gravity models and it was shown that the perturbation theory based template was able to reproduce the input value of $\log|f_{R0}|$ of the simulation in an unbiased way for $k < 0.1$ Mpc^{-1} [38].

C. Constraints on $f(R)$ gravity

We now present the results for constraints on $|f_{R0}|$, summarized in Table I. The Markov Chain Monte Carlo (MCMC) method is used to sample a probability distribution. The normalized distribution function of $\mathcal{L}/\mathcal{L}_{\max}$ of the chain is given in terms of $\log|f_{R0}|$ in the top panel of Fig. 4, and the $\Delta\chi^2$ is shown in the bottom panel.

We begin by analyzing our results while fixing G_Θ to the Planck ΛCDM model prediction of $G_\Theta = 0.46$. The measured $\log|f_{R0}|$ is then $\log|f_{R0}| < -3.87$ and $\log|f_{R0}| < -3.6$ at 68% and 95% confidence upper limits, respectively. The lower index denotes the prior is hit—recall the ΛCDM limit of $\log|f_{R0}| \lesssim -6$, and the upper indices denote 68% and 95% confidence levels of $\log|f_{R0}|$ represented by unbracketed and bracketed numbers, respectively. The distribution function and $\Delta\chi^2$ are presented by blue dashed curve in the left panel of Fig. 4.

The measured $\log f_{R0}$ after marginalizing G_Θ and all other parameters is $-4.5^{+0.96(1.4)}_{[\text{prior}]}$ as presented in Table I. The best fit $|f_{R0}|$ is 3.2×10^{-5}, and the upper bounds are $|f_{R0}| = 3.0 \times 10^{-4}$ and 8.0×10^{-4} at 68% and 95% confidence levels, respectively. The observed $\xi(\sigma, \pi)$ is presented as blue filled contours in Fig 3, and $\xi(\sigma, \pi)$ of the best fit $f(R)$ gravity model is represented as black dashed contours, which show a slightly better fit than $\xi(\sigma, \pi)$ of ΛCDM represented as black solid contours. The black solid curves in the left panel of Fig. 4 represent the distribution function (upper) and $\Delta\chi^2$ (lower). Note that $\log|f_{R0}| < -6$, i.e. ΛCDM, is within $\Delta\chi^2 < 1$ of our best fit value and so is wholly allowed by the current data. When $|f_{R0}|$ is larger than 10^{-4}, $\xi(\sigma, \pi)$ becomes significantly different from the

ΛCDM prediction. The black dotted contours in Fig. 3 represent $\xi(\sigma, \pi)$ with $|f_{R0}| = 3.0 \times 10^{-4}$ at 68% confidence bound. The difference from the measured $\xi(\sigma, \pi)$ can be observed.

In order to check the validity of our constraints, we test the effect of a different initial broadband shape of power spectra by using the WMAP9 best fit model as fiducial instead of Planck 2013. Although there is no significant difference within statistical allowances, the predicted initial broadband shape is slightly different in both cases. We would like to test whether this can cause a shift in the apparent f_{R0}. The black dashed curve in the right panel of Fig. 4 represents the likelihood function and $\Delta\chi^2$. The measured $\log|f_{R0}|$ using WMAP9 prior is $-4.6^{+0.81(1.2)}_{[\text{prior}]}$, which is consistent with the result using Planck 2013 prior. Thus our results do not appear to be biased by the CMB priors.

Finally, since we measure f_{R0} through its scale dependent effects, we consider a nontrivial scale dependent bias on our measurement. We model the bias as

$$b(k) = b_0 \frac{1 + A_2 k^2}{1 + A_1 k}. \tag{23}$$

This simple bias model, when implemented in the formula in Eq. (17), can nicely fit the N-body data of the halo power spectrum and extract correctly the linear growth rate on scales very relevant to the current analysis [56,57]. We find that the scale dependent bias parameters are determined as $A_2 = -0.8 \pm 4$ and $A_1 = -0.2 \pm 1.2$. Given the range of errors on these parameters and the range of wave numbers $k \lesssim 0.1$ Mpc^{-1}, the scale dependence of the bias is poorly determined. Since our established cutoff on small scales removes where scale dependent bias is expected to be most significant, all other measurements, including f_{R0}, remain similar to the results with scale independent bias. Thus the measurements shown in Table I are not modified much by a possible existence of this scale dependent galaxy bias.

D. Tests of ΛCDM model

Considering the constraints on the other fitting parameters, we can see if there is any evidence of deviations from ΛCDM model. Information on the late-time cosmological expansion is encoded in the distances along and transverse to the line of sight. The distance measurements are not affected by the scale dependent growth functions in $f(R)$ gravity models. In Sec. III, we varied the scale dependent growth function D_δ^+ and the growth rate D_Θ^+ and found that the BAO ring is invariant (see Fig. 2). As a consequence, there is little change in the measured D_A and H^{-1} from our previous result where scale independent growth functions are assumed [13]. The measured D_A is $D_A = 1428.0^{+30.1}_{-28.1}$ Mpc, and the measured H^{-1} is

$H^{-1} = 3157.5^{+190.6}_{-176.1}$ Mpc. The prediction of the ΛCDM model is indicated by the x in Fig. 5, and the measured values, with uncertainties, are presented as filled contours in the top-left panel. The ΛCDM prediction is within the 1-σ confidence level. The measured distances are consistent with the results using ΛCDM templates presented in the fifth column of Table I.

Although we vary galaxy bias b in the fitting procedure, it is degenerate with the variation of G_δ on quasilinear scales. Thus as previously stated we can regard the combined measurement of b and G_δ as a probe of G_b, whose measured value is $1.13^{+0.09}_{-0.08}$. Again there is little difference from the previous result of G_b using ΛCDM templates presented in the fifth column of Table I.
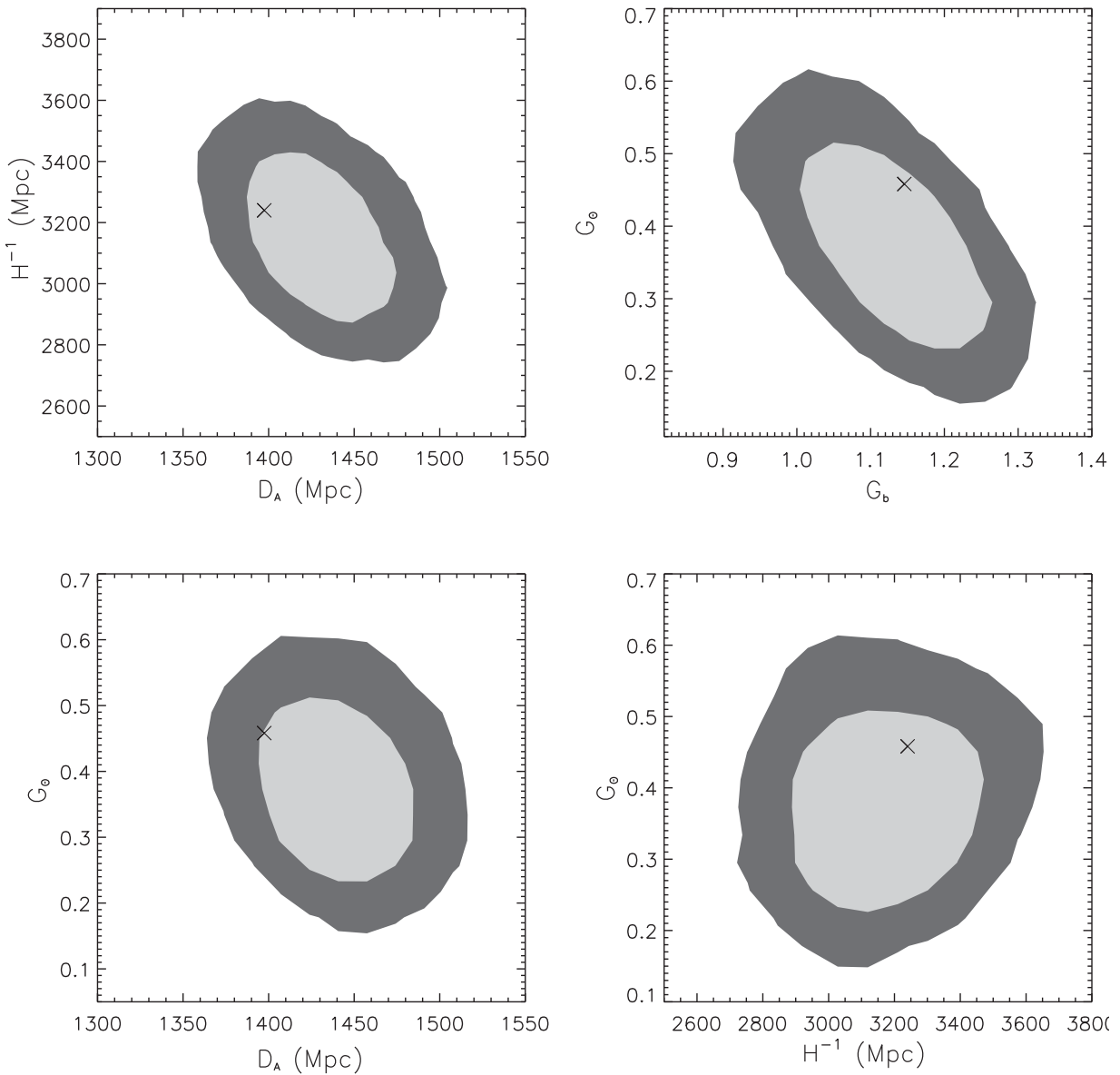

FIG. 5. The 2D joint likelihood contours at 68% and 95% CL measured for D_A, H^{-1}, G_b and G_Θ are shown, using $s_{cut} = 50\,h\,\mathrm{Mpc}^{-1}$ and $\sigma_{cut} = 40\,h\,\mathrm{Mpc}^{-1}$. The x denotes the Planck best-fit ΛCDM predictions (with G_b taking the value from fixing $f_{R0} = 0$).
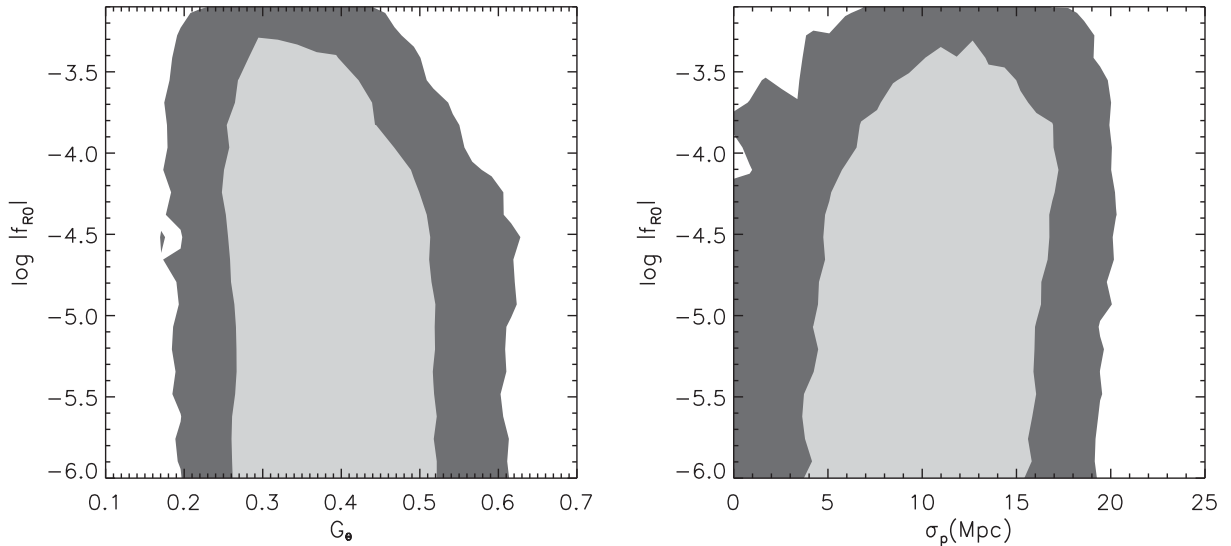
FIG. 6.   The 2D joint likelihood contours at 68% and 95% CL measured for $\log |f_{R0}|$ and G_Θ are shown in the left panel, and for $\log |f_{R0}|$ and σ_p are shown in the right panel, using $s_{\mathrm{cut}} = 50 \, h^{-1}$ Mpc and $\sigma_{\mathrm{cut}} = 40 \, h^{-1}$ Mpc.

When we fit the measured $\xi(\sigma, \pi)$, the amplitudes of the growth function and growth rate are determined at an effective scale $k^* \sim 0.07 \, h \, \mathrm{Mpc}^{-1}$ in our analysis. In $f(R)$ gravity the growth functions are enhanced in a scale dependent manner. Therefore if the amplitude of the growth function and growth rate at k^* are tuned to be nearly the same as the ΛCDM model (e.g. to agree with data), then the measured G_b and G_Θ must be smaller to offset the enhancement. So for appreciable $\log |f_{R0}|$ we expect an anticorrelation between $\log |f_{R0}|$ and G_Θ. This is visible in the left panel of Fig. 6 for the larger values of $\log |f_{R0}|$. Since the best fit $\log |f_{R0}|$ is slightly larger than the LCDM bound, this may contribute to why the measured $G_\Theta = 0.39^{+0.09}_{-0.09}$ is smaller than the ΛCDM result. However, the prediction of ΛCDM presented by the x in Fig. 5 is still within the 68% CL measured G_Θ contours.

Finally, we show the measured FoG effect in terms of σ_p in the right panel of Fig. 6. Again we do not find any significant change from the previous result using ΛCDM templates.

IV. CONCLUSION

We have investigated the effect of $f(R)$ gravity on the redshift space correlation function $\xi(\sigma, \pi)$ using a consistent modified gravity perturbation theory template that also includes some nonlinear and chameleon screening effects. The scale dependent growth functions D_δ^+ and D_Θ^+ alter at late times the initial broadband shape probed by the CMB experiments, but the comoving scale of the sound horizon is not affected, and we find the measured BAO ring remains the same as in ΛCDM and so the distances D_A and H^{-1} do also. The effect of modified gravity would be most evident in the redshift space distortions and hence anisotropy of the clustering.

We demonstrated how $\xi(\sigma, \pi)$ alters with increments of D_δ^+ and D_Θ^+ for small and large f_{R0} values in Fig. 2. This shifts the correlation amplitude at the BAO scale and other scales compared with the scale independent growth functions case. At small $|f_{R0}| = 3.2 \times 10^{-5}$, there is no significant anisotropic variation with ΔD_Θ^+; the peak locations move nearly coherently anticlockwise along the BAO ring. But when $|f_{R0}|$ increases and it becomes larger than $|f_{R0}| = 10^{-4}$, the effect of anisotropic amplification dominates and $\xi(\sigma, \pi)$ departs from ΛCDM.

Using the BOSS DR11 data we measure the anisotropic $\xi(\sigma, \pi)$, presented as blue filled contours in Fig. 3, and find a best fit $|f_{R0}| = 3.2 \times 10^{-5}$, with an upper bound $|f_{R0}| < 3.0 \times 10^{-4}$ at the 68% confidence level; the lower 68% confidence level is consistent with ΛCDM. We also note an anticorrelation between f_{R0} and the scale independent growth rate G_Θ that could reduce the measured value of G_Θ despite the enhancement of growth due to $f(R)$ gravity.

We tested our data analysis pipeline by applying it to ΛCDM mock catalogues, and we reproduced the ΛCDM bound of $|f_{R0}| \lesssim 10^{-6}$. We also tested the robustness of our results against the change of the CMB prior. There is a slight difference in the measured early broadband shape of spectra between WMAP9 and Planck 2013, but the measured $|f_{R0}|$ is independent of this difference. In addition, we tested the effect of the scale dependent bias on the measured $|f_{R0}|$. Again our results were shown to be insensitive to a possible scale dependent galaxy bias.

Although the best fit value of $|f_{R0}|$ is away from ΛCDM bound, the deviation is insignificant with $\Delta \chi^2 \lesssim 1$, and it is indistinguishable from ΛCDM model. The comparison of the measured minimum χ^2_{min} when marginalizing or fixing $\log |f_{R0}|$ to zero, and marginalizing or fixing the scale independent growth rate to the Planck best fit, are presented

in last row of Table I. With future wide, deep spectroscopy experiments such as Dark Energy Spectroscopy Instrument (DESI) we will be able to use the redshift space correlation function $\xi(\sigma, \pi)$ to probe $f(R)$ gravity below $|f_{R0}| < 10^{-4}$—and other scale dependent modified gravity—and test general relativity more stringently.

APPENDIX: POWER SPECTRUM AND BISPECTRUM CALCULATIONS IN RegPT

In this appendix, based on the RegPT treatment, we summarize the expressions for the basic ingredients needed to compute the redshift-space power spectrum in $f(R)$ gravity model [Eq. (17)]. The RegPT scheme is based on a multipoint propagator expansion, and with this scheme any statistical quantities consisting of density and velocity

fields are built up with multipoint propagators, in which nonperturbative properties of gravitational growth are wholly encapsulated [58]. Making use of the analytic properties of the propagators, a novel regularized treatment is constructed with the help of the standard PT kernels [59], showing that the proposed scheme can be used to give a percent-level prediction of the power spectrum and correlation function in the weakly nonlinear regime in both real and redshift spaces [42,44].

Let us define a two-component multiplet, $\Psi_a(\boldsymbol{k}; t) \equiv (\delta(\boldsymbol{k}; t), \Theta(\boldsymbol{k}; t))$. Then, the power spectra of Ψ_a valid at one-loop order are expressed as

$$
\begin{aligned}
P_{ab}(k; t) &= \Gamma_a^{(1)}(k; t)\Gamma_b^{(1)}(k; t)P_0(k) \\
&+ 2 \int \frac{d^3\boldsymbol{q}}{(2\pi)^3} \Gamma_a^{(2)}(\boldsymbol{q}, \boldsymbol{k} - \boldsymbol{q}; t)\Gamma_b^{(2)}(\boldsymbol{q}, \boldsymbol{k} - \boldsymbol{q}; t) \\
&\times P_0(q)P_0(|\boldsymbol{k} - \boldsymbol{q}|),
\end{aligned} \tag{A1}
$$

where P_0 is the power spectrum of initial density field δ_0. The functions $\Gamma_a^{(n)}$ are the multipoint propagators. For the one-loop calculation, the relevant expressions for the *regularized* propagators, which reproduce both the resummed behavior at high-k and standard PT results at low-k, are given by

$$
\begin{aligned}
\Gamma_a^{(1)}(k; t) &= \left[F_a^{(1)}(k; t)\left\{1 + \frac{k^2\sigma_{\rm d}^2}{2}\right\} \right. \\
&\left. + 3 \int \frac{d^3\boldsymbol{q}}{(2\pi)^3} F_a^{(3)}(\boldsymbol{k}, \boldsymbol{q}, -\boldsymbol{q}; t)P_0(q) \right] e^{-k^2\sigma_{\rm d}^2/2}
\end{aligned} \tag{A2}
$$

$$
\Gamma_a^{(2)}(\boldsymbol{q}, \boldsymbol{k} - \boldsymbol{q}; t) = F_a^{(2)}(\boldsymbol{q}, \boldsymbol{k} - \boldsymbol{q}; t)e^{-k^2\sigma_{\rm d}^2/2}, \tag{A3}
$$

where the functions $F_a^{(n)}$ are the standard PT kernels, sometimes written as $F_a^{(n)} = (F_n, G_n)$ [43]. Note that the leading-order kernel $F_a^{(1)}$ is related to the linear growth factor through $F_a^{(1)} = (D_+^\delta, D_+^\Theta)$. The quantity $\sigma_{\rm d}$ is the dispersion of the linear displacement field given by

$$
\sigma_{\rm d}^2 = \int \frac{dq}{6\pi^2} P_0(q)\{D_+^\delta(q; t)\}^2. \tag{A4}
$$

The above expressions are used to compute the power spectra $P_{\delta\delta}$, $P_{\delta\Theta}$, and $P_{\Theta\Theta}$ that explicitly appear in Eq. (17). We also need to evaluate the A and B terms, which implicitly depend on the power spectrum and bispectrum [see Eqs. (19) and (20)]. Since these terms are regarded as next-to-leading order, the tree-level calculation is sufficient for a consistent one-loop calculation of Eq. (17). Thus, the power spectrum and bispectrum in the A and B terms are evaluated with

$$P_{ab,\text{tree}}(k) = \Gamma_a^{(1)}(k)\Gamma_b^{(1)}(k)P_0(k), \qquad (A5)$$

$$B_{abc,\text{tree}}(\boldsymbol{k}_1, \boldsymbol{k}_2, \boldsymbol{k}_3) = 2\Gamma_a^{(2)}(\boldsymbol{k}_2, \boldsymbol{k}_3)\Gamma_b^{(1)}(\boldsymbol{k}_2)\Gamma_c^{(1)}(\boldsymbol{k}_3)$$
$$\times P_0(k_2)P_0(k_3) + (\text{cyc.perm}). \quad (A6)$$

The propagators $\Gamma_a^{(1)}$ and $\Gamma_a^{(2)}$ in the above are also evaluated with the tree-level expressions:

$$\Gamma_{a,\text{tree}}^{(n)}(\boldsymbol{k}_1, ..., \boldsymbol{k}_n; t) = F_a^{(n)}(\boldsymbol{k}_1, ..., \boldsymbol{k}_n; t)e^{-k^2\sigma_d^2/2}, \quad (A7)$$

where $k = |\boldsymbol{k}_{1\cdots n}|$.

Note finally that while the power spectrum and bispectrum given above are quite general and valid in any model of modified gravity, the expressions for the propagators in RegPT might receive some corrections. This issue has been discussed in detail in Ref. [10]. However, it has been found that within the $f(R)$ gravity model, any corrections due to the modification of gravity are very small and can be neglected at the large scales of our interest. Hence, all the expressions given above are basically the same as those in GR, except for the standard PT kernels, $F_a^{(n)}$. Unlike the GR case, the time and scale dependence of $F_a^{(n)}$ are not separately treated in $f(R)$ gravity model. The functional form of $F_a^{(n)}$ is thus nontrivial, even if the deviation of gravity from GR is small. In this paper, on the basis of Eqs. (2), (3), (6) and (7), we derive the equations that govern the standard PT kernels. Solving these equations numerically, we construct the kernels that are tabulated as function of wave vectors [60].

[1] C. Alcock and B. Paczynski, Nature (London) **281,** 358 (1979).
[2] N. Kaiser, Mon. Not. R. Astron. Soc. **227,** 1 (1987).
[3] Y.-S. Song and W. J. Percival, J. Cosmol. Astropart. Phys. 10 (2009) 004.
[4] E. V. Linder, Astropart. Phys. **29,** 336 (2008).
[5] Y. Wang, J. Cosmol. Astropart. Phys. 05 (2008) 021.
[6] S. Nesseris and L. Perivolaropoulos, Phys. Rev. D **77,** 023504 (2008).
[7] M. White, Y.-S. Song, and W. J. Percival, Mon. Not. R. Astron. Soc. **397,** 1348 (2009).
[8] Y. S. Song, W. Hu, and I. Sawicki, Phys. Rev. D **75,** 044004 (2007).
[9] Y. S. Song, H. Peiris, and W. Hu, Phys. Rev. D **76,** 063517 (2007).
[10] A. Taruya, T. Nishimichi, F. Bernardeau, T. Hiramatsu, and K. Koyama, Phys. Rev. D **90,** 123515 (2014).
[11] Y.-S. Song, T. Okumura, and A. Taruya, Phys. Rev. D **89,** 103541 (2014).
[12] E. V. Linder, M. Oh, T. Okumura, C. G. Sabiu, and Y.-S. Song, Phys. Rev. D **89,** 063525 (2014).
[13] Y.-S. Song, C. G. Sabiu, T. Okumura, M. Oh, and E. V. Linder, J. Cosmol. Astropart. Phys. 12 (2014) 005.
[14] P. A. R. Ade *et al.* (Planck Collaboration), arXiv:1502.01590.
[15] L. Samushia, B. A. Reid, M. White, W. J. Percival, A. J. Cuesta, G. B. Zhao, A. J. Ross, M. Manera *et al.*, Mon. Not. R. Astron. Soc. **439,** 3504 (2014).
[16] A. G. Sanchez, F. Montesano, E. A. Kazin, E. Aubourg, F. Beutler, J. Brinkmann, J. R. Brownstein, A. J. Cuesta *et al.*, Mon. Not. R. Astron. Soc. **440,** 2692 (2014).
[17] F. Beutler *et al.* (BOSS Collaboration), Mon. Not. R. Astron. Soc. **443,** 1065 (2014).
[18] J. Dossett, B. Hu, and D. Parkinson, J. Cosmol. Astropart. Phys. 03 (2014) 046.
[19] A. Johnson, C. Blake, J. Dossett, J. Koda, D. Parkinson, and S. Joudaki, arXiv:1504.06885.
[20] F. Simpson, C. Heymans, D. Parkinson, C. Blake, M. Kilbinger, J. Benjamin, T. Erben, H. Hildebrandt *et al.*, Mon. Not. R. Astron. Soc. **429,** 2249 (2013).
[21] D. Rapetti, C. Blake, S. W. Allen, A. Mantz, D. Parkinson, and F. Beutler, Mon. Not. R. Astron. Soc. **432,** 973 (2013).
[22] M. Cataneo, D. Rapetti, F. Schmidt, A. B. Mantz, S. W. Allen, D. E. Applegate, P. L. Kelly, A. von der Linden, and R. G. Morris *et al.*, Phys. Rev. D **92,** 044009 (2015).
[23] A. Terukina, L. Lombriser, K. Yamamoto, D. Bacon, K. Koyama, and R. C. Nichol, J. Cosmol. Astropart. Phys. 04 (2014) 013.
[24] H. Wilcox, D. Bacon, R. C. Nichol, P. J. Rooney, A. Terukina, A. K. Romer, K. Koyama, G. B. Zhao *et al.*, arXiv:1504.03937.
[25] G. B. Zhao, H. Li, E. V. Linder, K. Koyama, D. J. Bacon, and X. Zhang, Phys. Rev. D **85,** 123546 (2012).
[26] Y. S. Song, G. B. Zhao, D. Bacon, K. Koyama, R. C. Nichol, and L. Pogosian, Phys. Rev. D **84,** 083523 (2011).
[27] G. B. Zhao, T. Giannantonio, L. Pogosian, A. Silvestri, D. J. Bacon, K. Koyama, R. C. Nichol, and Y. S. Song, Phys. Rev. D **81,** 103510 (2010).
[28] S. F. Daniel, E. V. Linder, T. S. Smith, R. R. Caldwell, A. Cooray, A. Leauthaud, and L. Lombriser, Phys. Rev. D **81,** 123508 (2010).
[29] S. F. Daniel and E. V. Linder, Phys. Rev. D **82,** 103523 (2010).
[30] T. Giannantonio, M. Martinelli, A. Silvestri, and A. Melchiorri, J. Cosmol. Astropart. Phys. 04 (2010) 030.
[31] M. Raveri, B. Hu, N. Frusciante, and A. Silvestri, Phys. Rev. D **90,** 043513 (2014).
[32] E. Berti, E. Barausse, V. Cardoso, L. Gualtieri, P. Pani, U. Sperhake, L. C. Stein, N. Wex *et al.*, arXiv:1501.07274.
[33] K. Koyama, arXiv:1504.04623.
[34] D. J. Eisenstein *et al.* (SDSS Collaboration), Astron. J. **142,** 72 (2011).
[35] S. Alam *et al.* (SDSS-III Collaboration), Astrophys. J. Suppl. Ser. **219,** 12 (2015).

[36] K. Koyama, A. Taruya, and T. Hiramatsu, Phys. Rev. D **79**, 123512 (2009).

[37] A. Taruya, T. Nishimichi, and S. Saito, Phys. Rev. D **82**, 063522 (2010).

[38] A. Taruya, K. Koyama, T. Hiramatsu, and A. Oka, Phys. Rev. D **89**, 043509 (2014).

[39] J. C. Jackson, Mon. Not. R. Astron. Soc. **156**, 1 (1972).

[40] R. Scoccimarro, Astrophys. J. **517**, 531 (1999)

[41] R. Scoccimarro, Phys. Rev. D **70**, 083007 (2004)

[42] A. Taruya, T. Nishimichi, and F. Bernardeau, Phys. Rev. D **87**, 083509 (2013).

[43] F. Bernadeau, S. Colombi, E. Gaztañaga, and R. Scoccimarro, Phys. Rep. **367**, 1 (2002).

[44] A. Taruya, F. Bernardeau, T. Nishimichi, and S. Codis, Phys. Rev. D **86**, 103528 (2012).

[45] P. A. R. Ade *et al.* (Planck Collaboration), Astron. Astrophys. **571**, A16 (2014).

[46] A. S. Bolton, D. J. Schlegel, É. Aubourg *et al.*, Astrophys. J. **144**, 144 (2012).

[47] K. S. Dawson, D. J. Schlegel, C. P. Ahn *et al.*, Astrophys. J. **145**, 10 (2013).

[48] S. A. Smee, J. E. Gunn, A. Uomoto *et al.*, Astrophys. J. **146**, 32 (2013).

[49] D. G. York, J. Adelman, J. E. Anderson, Jr. *et al.*, Astrophys. J. **120**, 1579 (2000).

[50] J. E. Gunn, W. A. Siegmund, E. J. Mannery *et al.*, Astrophys. J. **131**, 2332 (2006).

[51] The data and random catalogues will be available online at http://data.sdss3.org/sas/dr11/boss/.

[52] S. E. Nuza, A. G. Sánchez, F. Prada *et al.*, Mon. Not. R. Astron. Soc. **432**, 743 (2013).

[53] S. D. Landy and A. S. Szalay, Astrophys. J. **412**, 64 (1993).

[54] M. Manera, R. Scoccimarro, W. J. Percival, L. Samushia, C. K. McBride, A. Ross, R. Sheth, M. White *et al.*, Mon. Not. R. Astron. Soc. **428**, 1036 (2013).

[55] B. A. Reid, L. Samushia, M. White, W. J. Percival, M. Manera, N. Padmanabhan, A. J. Ross, A. G. Sanchez *et al.*, Mon. Not. R. Astron. Soc. **426**, 2719 (2012).

[56] T. Nishimichi and A. Taruya, Phys. Rev. D **84**, 043526 (2011).

[57] T. Ishikawa, T. Totani, T. Nishimichi, R. Takahashi, N. Yoshida, and M. Tonegawa, Mon. Not. R. Astron. Soc. **443**, 3359 (2014).

[58] F. Bernadeau, M. Crocce, and R. Scoccimarro, Phys. Rev. D **78**, 103521 (2008).

[59] F. Bernadeau, M. Crocce, and R. Scoccimarro, Phys. Rev. D **85**, 123519 (2012).

[60] A. Taruya *et al.* (to be published).